Hydrology and Earth System Sciences Discussions

Global land-surface evaporation estimated from satellite-based observations

D. G. Miralles[1], T. R. H. Holmes[1,2], R. A. M. De Jeu[1], J. H. Gash[1],
A. G. C. A. Meesters[1], and A. J. Dolman[1]

[1]Department of Hydrology, VU University, Amsterdam, The Netherlands
[2]Hydrology and Remote Sensing Lab, USDA-ARS, Beltsville, MD, USA

Correspondence to: D. G. Miralles (diego.miralles@falw.vu.nl)

Title Page

Abstract	Introduction
Conclusions	References
Tables	Figures

◄◄	►►
◄	►
Back	Close

Full Screen / Esc

Printer-friendly Version

Interactive Discussion

Abstract

This paper outlines a new methodology to derive evaporation from satellite observations. The approach uses a variety of satellite-sensor products to estimate daily evaporation at a global scale, with a 0.25 degree spatial resolution. Central to this approach
is the use of the Priestley and Taylor (PT) evaporation model. Because the PT equation is driven by net radiation, this strategy avoids the need to specify surface fields of variables, such as the surface conductance, which cannot be detected directly from space. Key distinguishing features are the use of microwave-derived soil moisture, land surface temperature and vegetation density, as well as the use of a detailed rainfall interception module. The modelled evaporation is validated against one year of eddy covariance measurements from 43 stations. The estimated annual totals correlate well with the stations' annual cumulative evaporation ($R = 0.84$, $N = 43$) and show a negligible bias (-1.5%). The validation of the daily time series at each individual station shows good model performance in all vegetation types and climate conditions with an average correlation coefficient of $\overline{R} = 0.84$, still lower than the $\overline{R} = 0.91$ found in the validation of the monthly time series. The first global map of annual evaporation developed through this methodology is also presented.

1 Introduction

Detecting changes in the hydrological cycle is essential if we are to predict the impacts of climate change. However, climate change is acting on a dynamic three dimensional globe where changes in one region may produce impacts in another. Therefore there is a need to expand the current climate change studies to encompass the entire globe.

Precipitation and evaporation are the two key components of the global water cycle. Evaporation can cause feedbacks on large scale water processes (e.g. Poveda and Mesa, 1997) and affect the dynamics of the atmosphere due to changes in the Bowen ratio (e.g. Dow and DeWalle, 2000). While our capability of observing precipitation has

considerably improved with the deployment of dedicated satellites such as the Tropical Rainfall Measuring Mission (TRMM) and in the near future the Global Precipitation Measurement (GPM), our capability of observing the return-flow of moisture from the land to the atmosphere is still poor (Dolman and De Jeu, 2010). Model estimates put the amount of evaporation from the global land masses somewhere between 58–85 10^3 km^3 yr^{-1}, although the exact magnitude and spatial and temporal variability are still highly uncertain (Dirmeyer et al., 2006).

If we are to effectively manage adaptation to climate change, the uncertainty in predictions of future climate must be reduced. This creates the need for evaporation products that can be used to validate components of Global Circulation Models (GCM) and serve as an observational benchmark for GCM developers (Blyth et al., 2009). The development of evaporation data sets from hydrological models, land surface parameterisation schemes, and/or through the application of the currently available data products (including remote sensing data) are therefore essential to improve predictions of future climate.

In the last two decades several attempts have been made to build global evaporation products based on a range of approaches tailored to specific input data. They can be categorized in five groups depending on whether they are based on: (1) off line models (e.g. GSWP – Dirmeyer et al., 2006), (2) Penman-Monteith equation (Choudhury and DiGirolamo, 1998), (3) temperature change over time (e.g. ALEXI – Anderson et al., 1997), (4) Priestley-Taylor equation (Fisher et al., 2008), and (5) machine-learning algorithms on a combination of in situ observations, model results and remote sensing data (Jung et al., 2009). Not all of these approaches have been adapted to the global scale and daily frequency, and not all the results are publicly available. The majority of them lack the required emphasis on estimating rainfall interception loss and do not couple transpiration with observed soil moisture conditions. In addition, only a few of them (i.e. Fisher et al., 2008) include observation-based moisture constraints within their scheme. In 2008 the LandFlux-EVAL initiative of the GEWEX Radiation Panel raised the importance of evaluation and inter-comparison of the existing

land evapotranspiration products (Jimenez et al., 2009) towards the creation of reliable evaporation benchmarks.

The present paper outlines the methodology of a new model to estimate global land-surface evaporation entirely from satellite observations, with the ultimate goal of deriving a global 25 year, 0.25 degree, daily data set that can be used for studies of the global hydrological cycle. Central to this approach is the use of the Priestley and Taylor (PT) (1972) evaporation model. Because the PT equation is driven by net radiation, this strategy avoids the need to specify surface fields of variables, such as the surface conductance, which cannot as yet be detected from space directly. Key distinguishing features are the use of microwave derived soil moisture, land surface temperature and vegetation density. Another important feature is the detailed estimation of rainfall interception loss, a process that is often ignored yet typically associated with a large fraction of the uncertainty of global evaporation estimates (see Jimenez et al., 2010).

2 Model methodology

The model, known as GLEAM (Global Land surface Evaporation: the Amsterdam Model), is designed to maximize the use of satellite-derived observations to create a spatially coherent estimate of the evaporative flux over land. For this reason, parameterisations are chosen that have global validity; whenever possible, globally constant parameters are preferred over those which vary across the globe. As a consequence, the model distinguishes only three sources of evaporation based on the land surface type: (1) bare soil, (2) short vegetation, and (3) vegetation with a tall canopy. The snow and ice sublimation is estimated for the pixels covered in snow through a separate routine. The contribution of lakes and rivers is not modelled; the predicted evaporation therefore refers only to the land fraction of the total surface area of each grid cell. The land evaporation of each modelled grid-box is the sum of the actual evaporation as calculated for each of the three surface types (s), weighted by their fractional coverage (a):

Global land-surface evaporation

D. G. Miralles et al.

$$E = \sum_{s=1}^{3} E_{a,s}\, a_s. \tag{1}$$

The global model is composed of four modules. In the first module, the evaporation of intercepted rainfall from forest canopies is calculated. A separate module describes the water budget that distributes the incoming precipitation (rain and snow) over the root-zone. In a third module, the stress conditions are parameterised as a function of the root-zone available water and dynamic vegetation information. Finally, the evaporation from each of the three surface components is calculated, based on the PT equation, the modelled stress, rainfall interception and snow sublimation.

Figure 1 gives an overview of the structure of GLEAM and its main inputs and outputs. The interception model has already been described and validated by Miralles et al. (2010). The entire evaporation model is also validated in the present paper.

2.1 Rainfall interception loss

Previously, the evaporation from wet forest canopies, referred to as rainfall interception loss, has been thought to be one of the components of the evaporative flux associated with the most uncertainty (see Jimenez et al., 2010). In GLEAM, it is explicitly modelled according to Gash's analytical model (Gash, 1979; Valente et al., 1997). Following this approach, the volume of water that evaporates from the canopy is derived from the daily rainfall using parameters that describe the canopy cover, canopy storage, and mean rainfall and evaporation rate during saturated canopy conditions. The derivation of the parameters, validation and global implementation of the GLEAM interception model is fully described by Miralles et al. (2010).

The model is driven by remote sensing products and static parameters derived from literature values. A novelty in this approach is the use of a remotely sensed lightning frequency product to define global maps of monthly climatology of rainfall rate. Miralles et al. (2010) showed a strong correlation ($R = 0.86$) and a negligible bias between

Printer-friendly Version

Interactive Discussion

modelled and observed values of interception as reported in 42 field studies over different forest ecosystems.

2.2 Soil water content

The second module computes a daily running water balance that describes the evolution of root-zone moisture. It represents the soil moisture as a continuity relationship between water inputs (snowmelt and rainfall minus interception), and outputs (evaporation and percolation to deeper layers) over several soil layers. The water balance is calculated separately for the three land surface types, each with a different number of layers.

Acknowledging that the evaporation of water from soil is mainly controlled by the available energy and the soil moisture conditions, final estimates of evaporation will be highly dependent on the reliability of the precipitation data driving the soil water budget. In order to constrain the resulting uncertainty in modelled evaporation, microwave remote sensing data of surface soil moisture are used to correct the running water balance estimates at the daily time step using a Kalman filter assimilation approach based on the estimated uncertainty of the satellite observations.

2.2.1 Inputs to the soil water budget

The inputs to the soil water budget come exclusively from precipitation, both as rainfall and as snowfall. Even though irrigation is not included as an input, the subsequent assimilation of the satellite soil moisture will partly account for it by adjusting the soil moisture seasonal dynamics of the area.

Precipitation is divided into rainfall and snowfall depending on the satellite observations of snow depth (D_s); when D_s is over 10 mm (snow water equivalent), precipitation is considered snowfall (P_s). Rainfall (P_r) enters the soil directly, except for the fraction intercepted by tall canopies and evaporated back into the atmosphere (I). P_s however, does not enter the soil directly but accumulates in a layer on top of the soil column.

This snow can either evaporate as E_s (see Sect. 2.4), or melt and enter the soil water balance. The initial estimate of the snow depth (D_m^-) for a given day (i) is calculated as

$$D_{mi}^- = D_{mi-1} + P_{si} - E_{si}. \tag{2}$$

This initial estimate is compared with D_s. In the cases when the estimate exceeds the observed value, the difference is attributed to snow melt (F_s):

$$F_{si} = D_{mi}^- - D_{si}, \tag{3}$$

and the estimated snow depth is reduced to match the satellite observation:

$$D_{mi} = D_{si}.$$

The total flux of water into the soil water balance for day i is then calculated as

$$F_i = (P_{ri} - I_i) + F_{si}. \tag{4}$$

In this study, the entire water flux (F) infiltrates the soil column. With the intention of maintaining the simplicity of GLEAM, processes like surface overland flow (when the water flux exceeds the infiltration capacity of the soil) and bypass flow (when the water reaches the groundwater directly) are considered to have a negligible effect in the evaporation processes at the coarse resolution of the model. Therefore, no horizontal movement of water or routing between adjacent pixels is considered in the evaporation model.

2.2.2 Root-zone water balance

In nature, the depth of the soil column that affects the evaporation rate depends on the rooting depth of the vegetation, and may vary from a few centimetres for grasses to as deep as four metres for forests. For bare soil, the lack of roots limits the thickness of the layer that affects the evaporation rate to only a few centimetres. Because of those differences the model calculates the soil water balance is calculated for each land cover type individually.

The shallowest soil layer has a depth of 0–0.05 m, roughly corresponding to the sensing depth of the microwave soil moisture retrieval. For bare soil this shallow layer is the only layer considered. For short vegetation a second layer is defined from 0.05–1.00 m. For tall canopies two extra layers are defined (0.05–1.00 m and 1.00–2.50 m).

At each layer (l), the soil moisture content (w) on a given day (i) is modelled as:

$$w_i^{(l)} = w_{i-1}^{(l)} + \frac{F_i^{(l-1)} - E_{i-1}^{(l)} - F_i^{(l)}}{\Delta z^{(l)}}, \qquad (5)$$

where $F^{(l-1)}$ denotes the downward flux from the above layer, which in the case of the first layer will be the infiltration flux (F) calculated through Eq. (4). $E^{(l)}$ represents the removal of soil water due to evaporation, $\Delta z^{(l)}$ is the thickness of the layer and $F^{(l)}$ is the percolation flux to the next layer. $F^{(l)}$ is estimated as the volume of water exceeding the field capacity (w_{fc}), hence

$$F_i^{(l)} = \left(w_i^{(l)} - w_{fc} \right) \Delta z^{(l)}. \qquad (6)$$

The water percolating out of the deepest root-zone layer is assumed to be no longer available for plant uptake and therefore does not affect the modelled evaporation. Figure 2 presents an overview of the complete running water balance.

2.2.3 Satellite surface soil moisture assimilation

Satellite observations of soil moisture (θ) are assimilated with the modelled water content of the first soil layer ($w^{(1)}$) as predicted by Eq. (5). The approach follows a one-dimensional Kalman filter design (see Crow, 2007). Prior to the assimilation, the annual time series of satellite observations are normalised to match the mean and standard deviation of the annual time series of the model estimates with no Kalman filter update. Then the update of the model estimates at daily time step follows

$$w_i^{(1)+} = w_i^{(1)-} + K_i \left(\theta_i - w_i^{(1)-} \right), \qquad (7)$$

in which "−" and "+" denote values before and after the Kalman filter update. K represents the Kalman gain, which is calculated as

$$K_i = \frac{\Phi_i^-}{\Phi_i^- + S_i}, \tag{8}$$

where S denotes the error variance associated with the satellite observations (θ) and Φ^- is the background error variance of the Kalman filter forecasts. Φ^- is estimated as

$$\Phi_i^- = \Phi_{i-1}^+ + Q, \tag{9}$$

in which Q is the variance associated to the soil water balance estimates when propagated from time $i-1$ to i. Then Φ_i^- is also updated as

$$\Phi_i^+ = \Phi_i^- - K_i\,\Phi_i^-, \tag{10}$$

to obtain Φ^+, the variance error of the final estimates of soil moisture ($w^{(1)+}$).

In our approach we consider a constant value of $Q = 0.01$. This implies that the value of K will be fully determined by the estimation of the variance error in the microwave observations (S). According to De Jeu et al. (2008), the vegetation optical depth (τ) can be used to approximate the polynomial relation existing between the uncertainty of the microwave soil moisture retrieval and the vegetation density. This relation can be described as

$$S_i = \left(0.3\,\tau_i^{1.5} + 0.04\right)^2. \tag{11}$$

The microwave soil moisture observations are obtained nearly every day when the temperatures are above freezing. Pixels covered by snow, presenting a fraction of open water larger than 20%, or those which show an annual negative correlation coefficient between time series of satellite observations and model estimates (with no Kalman filter) are not subject to this assimilation. The impact of this assimilation is explored in Sect. 4.1 by comparison to in situ measurements of soil moisture.

Global land-surface evaporation

D. G. Miralles et al.

2.3 Evaporative stress

For most of the land surface, the actual evaporation rarely – if at all – reaches the potential rate due to suboptimal environmental conditions. In those cases the actual evaporation will be less than the maximum rate for a given ecosystem. Environmental factors limiting the potential evaporation can be: a lack of available soil water, seasonal or occasional decrease in biomass content, and extreme temperatures. To account for these effects it is common to define an empirical parameter (see for instance Barton, 1979) referred as the evaporation stress factor (S), with unity indicating no stress, and zero indicating maximum stress.

In GLEAM, S is parameterised separately for tall canopies, short vegetation, and bare soil. This parameterisation is based on the soil moisture conditions, and (for the herbaceous fraction) a parameter accounting for the development of vegetation over the year (vegetation optical depth, τ).

The soil moisture component of S is determined by the water content of the wettest soil layer as determined by the soil water module (see Sect. 2.2). This concept reflects the ability of vegetation to draw water from any layer within the root zone, and affects the tall canopy fraction (with three layers of soil) and short vegetation (with two soil layers), but not bare soil (which presents only one layer of soil). For soil moisture values below wilting point (w_{wp}), the stress is the maximum ($S = 0$); for values above the critical moisture level (w_c), there is no stress ($S = 1$). Between w_{wp} and w_c the stress increases as soil moisture decreases following a parabolic function for the fraction of tall canopy, and an exponential relation for the fraction of herbaceous and bare land cover (see Gouweleeuw, 2000). The stress functions for the three land-surface components according to these parameterisations are defined and illustrated in Fig. 3.

The development of vegetation over the growing season as affected by environmental conditions and plant health is not modelled explicitly. Instead, a satellite-derived parameter, the microwave vegetation optical depth (τ), is used as a proxy for the vegetation density because of its close relation to vegetation water content (De Jeu et al.,

2008). In this study τ is used in the herbaceous fraction to introduce the effect of seasonal or occasional changes in biomass content (i.e. because of harvesting, fires, etc.) into the final estimates of evaporation (see Fig. 3). Therefore, an important implication of using this dynamic estimate of vegetation density is that it adds variation to the otherwise static maps of cover fractions.

As an extra limit to the evaporative flux, the modelled evaporation is compared with the available water above w_{wp} according to the soil water module (see Sect. 2.2). This assures no evaporation is extracted below w_{wp} or from deep layers outside the root-zone.

2.4 Actual evaporation

Priestley and Taylor (1972) showed that the Bowen ratio would approach a constant value when air moves over a moist surface and gradients of temperature and specific humidity with height are small or the air becomes saturated with respect to moisture. The Priestley-Taylor (PT) equation has been shown to work well over many vegetation types with only small modifications. The formula calculates daily evaporation as a function of the available energy – net radiation (R_n) minus ground heat flux (G) – and a dimensionless coefficient (α) that parameterises the resistance to evaporation. Considering values of α for optimal environmental conditions (zero evaporative stress), the model can be applied to describe the potential latent heat flux, λE_p (MJ m^{-2}), as:

$$\lambda E_p = \alpha \frac{\Delta}{\Delta + \gamma} (R_n - G), \tag{12}$$

where Δ is the slope of the temperature/saturated vapour pressure curve (kPa K^{-1}) and γ is the psychrometric constant (kPa K^{-1}). λE_p can be divided by the latent heat of vaporization, λ (kJ kg^{-1}), calculated as a function of air temperature (Henderson-Sellers, 1984) to get the mass flux, which in turn is divided by the density of water ($\rho_w = 10^3$ kg m^{-3}) to derive potential evaporation (E_p) in mm day^{-1}. The magnitude of

G is approximated in GLEAM as a fraction of R_n, being 5%, 20% and 25% for the fraction of tall canopy, herbaceous and bare soil respectively.

For optimal environmental conditions (when actual equals potential evaporation), the value of $\alpha = 1.26$ is well-documented in the literature for grasslands. Similar values have also been found in past studies over bare lands (Owe and Van de Griend, 1990; Caylor et al., 2005). However, Shuttleworth and Calder (1979) found that a value of $\alpha = 0.72$ better reflected the conservative transpiration from forests; this value was estimated for two forest stands in the UK, where soil moisture deficit could be considered low although no parameterisation of the stress due to soil moisture conditions was performed. In 1984, Shuttleworth et al. found that a value of $\alpha = 0.91$ better suited the parameterisation of forest potential evaporation in a tropical region. In GLEAM, a constant value of $\alpha = 0.8$ is used to parameterise the tall canopy fraction, while a value of $\alpha = 1.26$ is applied in both the herbaceous and bare fractions.

As a result of suboptimal environmental conditions (due to soil water deficit or biomass changes), the volume of actual evaporation (E) is generally lower than the potential evaporation (E_p) calculated through Eq. (12). Several studies in the past (see for instance Barton, 1979) introduce the evaporation stress factor (S) to adapt the PT equation and account for the effect on E of suboptimal environmental conditions (see Sect. 2.3 for the parameterisation of S in GLEAM). In addition, when the canopy is wet the evaporation from tall canopies is not well described by the PT equation. In GLEAM, canopy rainfall interception is calculated independently (see Sect. 2.1). As a consequence of this separate estimation, the transpiration as calculated by Eq. (12) needs to be corrected by a fraction (β) of the interception loss (I) to avoid the double counting of evaporation for those hours with wet canopy. Taking this correction into consideration, and adding the evaporation from the wet forest canopy and the effect of the evaporative stress, GLEAM describes E (in mm day^{-1}) as:

$$E = S\,E_p + I - \beta\,I, \tag{13}$$

where β is considered a constant ($\beta = 0.07$ – Gash and Stewart, 1977). For the fractions of herbaceous and bare soil, the I term in Eq. (13) is zero.

Finally, the evaporation from snow-covered surfaces is calculated by adapting Δ and γ in the PT equation according to Murphy and Koop (2005). Literature values of α for snow-covered surfaces were not found and, therefore, α was calibrated based on 12 selected FLUXNET sites, each with more than fifty days of snow cover. It was found that $\alpha = 0.95$ minimized the average error in cumulative sublimation for all sites. Due to the sufficient availability of water, these ecosystems are considered to be unstressed, and values of $\alpha = 0.95$ and $S = 1$ are used as global constants for ice and snow pixels in the model.

3 Satellite observations

The driving data for the global hydrological model are listed in Table 1. All these data sets are primarily based on satellite observations. They are acquired from various sources and comprise well-validated products. Only the microwave vegetation optical depth represents a research product with limited validation. Its use in GLEAM for the parameterisation of the evaporative stress (Sect. 2.3) and the estimation of the uncertainty of satellite soil moisture observations (Sect. 2.2.3) is a unique feature of the proposed approach. The majority of the data sets are available at 0.25 degree regular grids; all the data sets presenting a different spatial resolution are re-gridded to a common 0.25 degree grid by means of Shepard's Method of inverse distance weighted interpolation (Shepard, 1968).

3.1 Net radiation

R_n is the principal driver of the latent heat flux and the main input for the estimation of λE_p by the PT equation (see Eq. 12). The NASA/GEWEX Surface Radiation Budget (SRB) Release-3.0 contains global daily averages of surface longwave and shortwave radiative variables on a $1° \times 1°$ grid. The data were obtained from the NASA Langley Research Center, Atmospheric Sciences Data Center NASA/GEWEX SRB

Project. The product is based on a range of satellite instruments, reanalysis and assimilation.

3.2 Precipitation

The water balance described in Sect. 2.2 is driven by P as retrieved according to the Climate Prediction Center morphing technique (CMORPH) and provided by Joyce et al. (2004). This technique uses half-hourly infrared observations – Geostationary Operational Environmental Satellite (GOES), the Geostationary Meteorological Satellite (GMS) and Meteosat – to propagate higher quality microwave precipitation estimates from the Advanced Microwave Sounding Unit-B (AMSU-B), the Special Sensor Microwave Imager (SSM/I), the TRMM Microwave Imager (TMI) and the Advanced Microwave Scanning Radiometer (AMSR). Between measurements, intensity and shape of the microwave-observed precipitation are modified by a time-weighted interpolation (morphing) resulting in a high spatial (0.07°) and temporal (30 min) resolution. In spite of a reported slight positive bias in summer and negative in winter (especially in high latitudes – see Zeweldi and Gebremichael, 2009), validation studies show better correlation with ground measurements than most of the currently available satellite-derived precipitation products (Ebert et al., 2007).

The spatial coverage of CMORPH is from 60° N to 60° S. For the latitudes outside this domain, the 1° daily Global Precipitation Climatology Project (GPCP-1DD) precipitation product is used (Huffman et al., 2001). It is produced by merging precipitation estimates from microwave, infrared, and sounder data observed by the international constellation of precipitation-related satellites, and precipitation gauge analyses (Huffman et al., 1997). GPCP-1DD has been widely used in different studies during the last few years as it represents one of the best available global precipitation products (Crow, 2007).

In GLEAM, GPCP estimates are scaled to match the annual density function and daily global mean of CMORPH at daily time step. Neither CMORPH nor GPCP distinguish between rain and snow, and for this reason the observed snow depth is used

to categorise precipitation as snowfall when the snow water-equivalent depth exceeds 10 mm instead of the default classification as rainfall (see Sect. 3.3).

3.3 Microwave retrievals

An increasing number of geophysical land surface variables are successfully being re-
trieved from satellites carrying passive microwave radiometers. In general, microwave retrievals have the benefit of being insensitive to clouds, resulting in a reliable twice-daily sampling rate. GLEAM relies heavily on four of those variables, as derived from the AMSR-E radiometer on the AQUA satellite: surface soil moisture (θ), land surface temperature (T), vegetation optical depth (τ) and snow depth (D_s). The mean spa-
tial resolution of the AMSR-E radiometer is between 12 km for the 36.5 GHz channel and 56 km for the 6.9 GHz channel. The first three parameters are derived with the Land Parameter Retrieval Model (LPRM) (Owe et al., 2008). LPRM is an iterative op-timization and polarization index-based retrieval model that uses the dual polarization channels at a single low microwave frequency to derive θ and τ. In this paper the com-
bined version (v04d) is used, in which the default 6.9 GHz based retrieval is replaced by the 10.7 GHz based product in areas that suffer from high levels of radio frequency interference in the lower band. The LPRM soil moisture product has been validated in several studies and is estimated to have an average accuracy of 0.06 m^3 m^{-3} (see De Jeu et al., 2008).
Even though the measured microwave vegetation optical depth has a direct relation with vegetation water content (Kirdiashev et al., 1979), it represents a pixel-averaged value. In this study, τ is assigned to each of the three land cover fractions based on two assumptions: (1) τ for the bare soil fraction is zero, and (2) τ for the short vegetation fraction is 60% of that of the tall canopy fraction. A five day central moving average is
calculated in order to gap-fill the data over a global domain and long gaps in wintertime are filled with the 10th percentile of the values measured in a specific grid cell over the year.

Full Screen / Esc

Printer-friendly Version

Interactive Discussion

LPRM uses the Ka-band vertical polarised channel to retrieve the physical temperature of the emitting surface, a method recently described by Holmes et al. (2009). The temperature retrieval is limited to the non-frozen land surface, and so by extension are all LPRM products. Under frozen conditions the temperature is not retrieved from microwave data; for that reason GLEAM uses the air temperature from the International Satellite Cloud Climatology Project (ISCCP) (Zhang et al., 2004) to gap-fill the data.

Finally, the strong effect that snow has on the microwave emission is used by the National Snow and Ice Data Center (NSIDC) to retrieve snow depth. In this study we use the AMSR-E/Aqua daily L3 global snow water equivalent EASE-Grids V001 (Kelly et al., 2003).

3.4 Static data sets

A limited number of static data sets are used in the global model. The most important one is the global Vegetation Continuous Fields product from MODIS, MOD44B (Hansen et al., 2005) which describes every pixel as a combination of its fractions of tall canopy, herbaceous vegetation and bare soil. The global fields of porosity (Φ) from FAO's world soil database (FAO, 2000) are used to define the values of wilting point, critical soil moisture and field capacity ($w_{wp} = \Phi - 0.35$, $w_c = \Phi - 0.2$ and $w_{fc} = \Phi - 0.1$ respectively); this data set is also used in the definition of θ (see Owe et al., 2008). For the interception loss model, information to determine the mean rainfall rate is derived from the Combined Global Lightning Flash Rate Density monthly climatology from NASA (Mach et al., 2007). Finally, a digital elevation model is used to calculate the air pressure as it varies with height above sea level according to the barometric formula and in accordance with the standard atmosphere.

4 Validation and discussion

The study presented here corresponds to the application of GLEAM for the year 2005. A two-year period (2003–2004) is used to spin up the soil water model. Both the soil moisture profile and the final estimates of evaporation are validated using in situ
5   measurements. This exercise is complementary to the independent validation of the GLEAM interception loss estimates presented by Miralles et al. (2010).

4.1 Soil moisture profile validation

In situ measurements of water content from a selection of stations from the Soil Climate Analysis Network (SCAN) are used to validate the daily soil moisture profile as
10   modelled for the corresponding pixels. SCAN stations present soil moisture sensors at depths of 0.05, 0.1, 0.2, 0.5 and 1.0 m. Only SCAN stations with continuous measurements during the year 2005 are selected for this validation. These stations are located in grasslands or other short vegetation ecosystems and therefore only the modelled soil moisture for the herbaceous fraction is used in this validation exercise. The Pear-
15   son's correlation coefficients between daily-averaged in situ measurements and modelled soil moisture content for the root-zone layers 1 and 2 ($w^{(1)}$ and $w^{(2)}$ respectively) are calculated at each station for the year 2005. Estimates of $w^{(1)}$ are compared with ground measurements at 5 cm; $w^{(2)}$ is compared with the average of the measurements at 0.05, 0.1, 0.2, 0.5 and 1.0 m.
20   Table 2 describes the stations used in this study as well as the individual correlations found between in situ measurements and GLEAM estimates of soil moisture. The mean correlation coefficients for a total sample of 30 stations are 0.60 and 0.69 for the first and second layer respectively. The histogram for the first layer is presented in Fig. 4a, which also illustrates the effect of the assimilation of θ into the profile. Figure 4b shows
25   the same inferences but for the second layer of soil.

An increase in the correlation in the first layer of soil is shown for 21 of the 30 stations when θ is assimilated (in the surface layer). Even though the second layer is not subjected to the assimilation scheme, the Kalman filter update of $w^{(1)}$ is likely to have an impact on today's S. This may affect tomorrow's root-zone moisture profile not only by altering the initial $w^{(1)}$ but also by changing the volume of water removed from the profile through E (see Sect. 2.4). However, the improved characterization of $w^{(1)}$ is shown to have little effect on the time series of $w^{(2)}$. This is mainly related to the fact that the lower thickness of the first layer makes variations in this layer cause only subtle changes in the rest of the profile.

4.2 Validation of evaporation estimates

4.2.1 Selection of ground stations

The modelled evaporation has been compared with eddy covariance measurements at a sample of FLUXNET stations for the year 2005. FLUXNET is a global network of micrometeorological towers (see Baldocchi et al., 2001) with the principal aim of quantifying carbon fluxes. At each station the evaporation flux is also measured using the eddy covariance technique, which samples a distance of 100 to 2000 m upwind of the tower. Given that the method is generally unreliable during rainfall, for this validation exercise we compare the modelled E without the I component (note that Miralles et al., 2010, have already validated the GLEAM interception loss product against a set of independent mass balance evaporation measurements).

FLUXNET stations are mainly located in Europe and the US, but cover the most common vegetation types and climates. For the purpose of this validation a station by station quality check was performed based on: (a) the amount of gap-filling in each daily aggregate (only days in which less than 10% of the half hourly data to form the aggregate were gap-filled), (b) the subsequent availability of daily data for the study period (only stations with a coverage of at least 60% of the days in 2005), and (c) the quality of their energy balance closure (only stations with less than 50% mismatch in

their energy closure). This yielded a total of 43 reliable FLUXNET sites covering a large variety of land surfaces. In the analysis below, these 43 stations are grouped based on the type of vegetation cover (low vegetation or tall canopy) and the volume of annual precipitation for the year 2005 according to CMORPH (dry: $P <= 500\,\text{mm}$, wet: $P > 500\,\text{mm}$), resulting in four functional groups. Therefore we distinguish between group: (A) tall canopy and wet climate ($N = 10$ stations), (B) tall canopy and dry climate ($N = 9$), (C) short vegetation and wet climate ($N = 13$), and (D) short vegetation and dry climate ($N = 11$). Table 3 presents the list of the 43 stations and their corresponding groups for the validation exercise.

4.2.2 Point versus pixel aspects

The ground measurements are essentially point measurements when compared to the corresponding 0.25 degree resolution pixels of GLEAM-modelled E. The model takes into account different surface types, short vegetation, tall canopy, and bare soil, and therefore accounts for sub-pixel heterogeneity to a certain extent. In this validation analysis the ground observations are compared with the modelled E corresponding to the specific land surface type associated with the site. However, the driving data consist of uniform values for the whole grid box. Especially in the case of R_n this may be an important obstacle for the comparison with site data as the spatial resolution is the lowest (1 degree) of all primary input data and since the energy budget is highly dependent on the particular characteristics of the surface (e.g. albedo). Moreover, the weight of R_n in the PT equation guaranties the propagation of these uncertainties and makes R_n the most crucial input in the estimation of E; in wet areas presenting low values of S, R_n is responsible for the majority of uncertainty in the final GLEAM E estimates. In order to better compare the relative merits of the evaporation model over different vegetation types – and reduce the magnitude of the uncertainties related to the driving data – we also report the results of a model run that substitutes the station-measured R_n for the satellite-based R_n.

Title Page

Abstract | Introduction

Conclusions | References

Tables | Figures

|◄ | ►|

◄ | ►

Back | Close

Full Screen / Esc

Printer-friendly Version

Interactive Discussion

4.2.3 Time series validation

The statistics of the validation of the daily time series of E are summarized in a Taylor diagram (Taylor, 2001) in Fig. 5a. For each of the four groups described in Sect. 4.2.1, this figure displays the average correlation coefficient, standard deviation and RMSD of
5 the stations within the group. Both standard deviation and RMSD are normalised using the corresponding station as a reference, and therefore the point denoted as "Ref" represents the location in the diagram of the time series of every station. The origin of the arrows indicates the results using the satellite-based R_n as input and the point of the arrows indicates the statistics with the site-measured R_n as input. As expected a
10 general improvement in the correlation and reduction of the magnitude of the residuals is found; this improvement is unambiguous in wet regions (groups A and C), in which evaporation is determined by the available energy. For the groups A and D, the slight overestimation of the variance is also corrected when we substitute the site-measured R_n for the satellite R_n. Unless otherwise noted, in the following only the results using
15 the site-measured R_n are discussed.

In the second Taylor diagram (Fig. 5b) the results of the validation of E estimates at daily time step are compared with the results of the monthly averages. Unsurprisingly, the averaging of the daily evaporation over the whole month results in an improvement of the model statistics, especially in terms of correlations. In group A this improvement
20 is more subtle due to the small amplitude of the seasonal cycle found in tropical forests; the station in Amazonia is the only one of the 43 stations that shows degradation in R. As it can be appreciated in Table 3 (which presents the values of the correlation coefficients for the individual locations in the two right columns), the Amazonian site on its own is responsible for the lower average correlation coefficient for group A found in
25 Fig. 5.

Overall, there is a high correspondence of GLEAM estimates with FLUXNET observations for each of the four groups, both for daily and monthly time series; the average correlation for the 43 stations is $\overline{R} = 0.84$ for the daily and $\overline{R} = 0.91$ for the monthly

series. Both the transpiration from tall canopies and short vegetated ecosystems seems to be equally well characterised by the model. Moreover, the extra complexity introduced by the modelling of evaporation stress does not seem to have a negative effect in the performance of the model over dry regions (group B and D). In any case, it is important to note that the presumed larger amplitude of the seasonal cycle of the evaporation in these regions is likely to have a positive effect on the correlation coefficients. Stations in group C present a high average correlation with FLUXNET data ($\overline{R} = 0.87$ for the daily and $\overline{R} = 0.93$ for the monthly time series), in agreement with the original intention of the Priestley-Taylor method to estimate evaporation from short unstressed vegetation. However, for group C, GLEAM overestimates the variability of the site measurements in average by 9% according to the daily time series and 11% for the monthly aggregates.

4.2.4 Annual totals and bias

With the aim of providing an insight into the bias for each of the four groups, Fig. 6 compares the total modelled and measured E for 2005 at each of the 43 FLUXNET stations. Overall the correlation coefficient shows a value of $R = 0.84$ and the bias is as low as -1.5% (which represents an average annual underestimation of 5.9 mm). Moreover, it can be noted that none of the different groups show major annual bias; this indicates that the scatter in Fig. 6 is not a response to systematic errors in the parameterisation of the two different vegetation types or the two climate conditions considered to define the four groups. Nevertheless, the annual bias at some of the stations can become important and it ranges between -35% to $+56\%$. The standard deviation of the bias is therefore high (25%), as can be seen from the value of RMSE $= 98\,\mathrm{mm\,yr^{-1}}$.

5 Global application of the model

The total evaporation for 2005 as modelled by GLEAM is presented in Fig. 7. The spatial patterns appear reasonable and the range of values corresponds well with previous attempts to estimate global evaporation (see Jimenez et al., 2009). A detailed study of the spatial distribution of the GLEAM-modelled E is the topic of planned future studies that will analyse the magnitude of the latent heat flux at a global scale, its seasonal variability, the relative importance of rainfall interception loss, the generation of water available for runoff and the physical processes controlling transpiration over the different regions of the world.

6 Conclusions

Evaporation remains the biggest unknown within the global hydrological fluxes; improved representation of its global dynamics is essential to produce a better understanding of the expected acceleration of the hydrological cycle. There have been several recent efforts towards the development of observation-based estimates of global evaporation; these attempt to create independent, daily-data driven benchmarks for GCM developers to improve their predictions of future climate. GLEAM (Global Land surface Evaporation: the Amsterdam Model) represents a new methodology that combines the wide range of currently existing satellite-sensor products to estimate reliable fields of daily global evaporation at a 0.25 degree spatial resolution. Because the approach is based on the Priestley and Taylor (1972) radiation-driven evaporation model, it avoids the need to specify spatially-varying surface fields that cannot be detected from space (like aerodynamic and stomatal resistance). The applicability of GLEAM relies exclusively on the availability of a suite of remotely-sensed input data products. Its simple strategy allows the application of the model, not only at a global scale (i.e. studies of trends in evaporation, evaluation of GCMs' performance, etc.), but also at a watershed scale through the utilisation of better resolution input data (i.e. radiometers,

in situ observations, etc.). Its minimal dependence on static fields of variables makes the quality of the evaporation estimates rely on the accuracy of the satellite inputs, and – unlike many other models – avoids the need for parameter tuning.

A major distinguishing feature of the approach is the detailed estimation of satellite-derived global fields of forest rainfall interception. Other characteristics are the coupling of the radiation-driven transpiration to the ground bio-physical processes (due to the parameterisation of the root-zone evaporative stress condition), and the separate estimation of bare soil evaporation and snow sublimation.

Model estimates have been successfully compared with ground data from a wide range of ecosystems. The two main intermediate products of GLEAM have been individually validated: the forest rainfall interception ($R = 0.86$, Bias = -0.6%, $N = 42$ – in Miralles et al., 2010) and the root-zone soil moisture ($\overline{R} = 0.60$ and $\overline{R} = 0.69$ for surface and deep layers respectively). In addition, final evaporation estimates have been validated against one year of eddy covariance measurements from 43 FLUXNET stations. Results show a high average correlation with ground measurements, both at a daily ($\overline{R} = 0.84$) and a monthly ($\overline{R} = 0.91$) time scale. Moreover, no systematic bias for specific vegetation types or rainfall conditions has been detected.

Updates to the model methodology are planned in the assimilation of remotely-sensed soil moisture data. These updates include the characterisation of the variance of soil water balance estimates (Q), and the assimilation of satellite observations into deeper layers to better propagate the optimisation through the entire root-zone. Other priorities include the use of higher resolution net radiation data and improved soil texture maps.

In an ongoing study we analyse the spatial distribution and magnitude of the global estimates of latent heat flux, and their seasonal variability and relative importance of their different components; this includes an insight into the global distribution of the evaporation drivers and the generation of water available for runoff. Our ultimate goal is to extend the time period to produce a global 0.25 degree daily evaporation data set spanning the modern satellite era spanning from 1983 to present. This exercise will

Back | Close

Full Screen / Esc

Printer-friendly Version

Interactive Discussion

need to take account of the availability of different data sets over time. The extended evaporation product will be described and compared with other existing products in forthcoming studies integrated within the LandFlux-EVAL initiative, and will be made available in the VU University Amsterdam geoservices website: http://geoservices.falw.vu.nl.

References

Anderson, M. C., Norman, J. M., Diak, G. R., Kustas, W. P., and Mecikalski, J. R.: A two-source time-integrated model for estimating surface fluxes using thermal infrared remote sensing, Remote Sens. Environ., 60, 195–215, 1997.

Anthoni, P. M., Knohl, A., and Rebmann, C.: Forest and agricultural land use dependent CO_2 exchange in Thuringia, Germany, Global Change Biol., 10, 2005–2019, 2004.

Ammann, C., Flechard, C., Leifeld, J., Neftel, A., and Fuhrer, J.: The carbon budget of newly established temperate grassland depends on management intensity, Agr. Ecosyst. Environ., 121, 5–20, 2007.

Baldocchi, D. D., Falge, E., Gu, L., et al.: FLUXNET: A new tool to study the temporal and spatial variability of ecosystem-scale carbon dioxide, water vapor, and energy flux densities, B. Am. Meteorol. Soc., 82, 2415–2434, 2001.

Baldocchi, D. D., Xu, L., and Kiang, N.: How plant functional-type, weather, seasonal drought, and soil physical properties alter water and energy fluxes of an oak-grass savanna and an annual grassland, Agr. Forest Meteorol., 123, 13–39, 2004.

Barton, I. J.: A parameterization of the evaporation from nonsaturated surfaces, J. Appl. Meteorol., 18, 43–47, 1979.

Bergeron, O., Margolis, H. A., Black, T. A., Coursolle, C., Dunn, A. L., Barr, A. G., and Wofsy, S. C.: Comparison of carbon dioxide fluxes over three boreal black spruce forests in Canada, Global Change Biol., 13, 89–107, 2007.

Global land-surface evaporation

D. G. Miralles et al.

Title Page

Abstract	Introduction
Conclusions	References
Tables	Figures

◀ | ▶

◀ | ▶

Back | Close

Full Screen / Esc

Printer-friendly Version

Interactive Discussion

Blyth, E. M., Shuttleworth, W. J., and Harding, R. J.: Summary of the GEWEX International Symposium on Global Land-surface Evaporation and Climate, Hydrol. Process., 23, 3411–3412, 2009.

Casal, P., Gimeno, C., Carrara, A., López-Sangil, L., and Sanz, M. J.: Soil CO_2 efflux and extractable organic carbon fractions under simulated precipitation events in a Mediterranean Dehesa, Soil Biol. Biochem., 41, 1915–1922, 2009.

Caylor, K. K., Shugart, H. H., and Rodriguez-Iturbe, I.: Tree canopy effects on simulated water stress in southern African savannas, Ecosystems, 8, 17–32, 2005.

Choudhury, B. J. and DiGirolamo, N. E.: A biophysical process-based estimate of global land surface evaporation using satellite and ancillary data; I. Model description and comparison with observations, J. Hydrol., 205, 164–185, 1998.

Cook, B. D., Davis, K. J., Wang, W., Desai, A. R., Berger, B. W., Teclaw, R. M., Martin, J. G., Bolstad, P. V., Bakwin, P. S., Yi, C., and Heilman, W.: Carbon exchange and venting anomalies in an upland deciduous forest in northern Wisconsin, USA, Agr. Forest Meteorol., 126, 271–295, 2004.

Crow, W. T.: A novel method for quantifying value in spaceborne soil moisture retrievals, J. Hydrometeorol., 8, 56–67, 2007.

Da Rocha, H. R., Manzi, A. O., Cabral, O. M., Miller, S. D., Goulden, M. L., Saleska, S. R., Restrepo-Coupe, N., Wofsy, S. C., Borma, L. S., Artaxo, P., Vourlitis, G., Nogueira, J. S., Cardoso, F. L., Nobre, A. D., Kruijt, B., Freitas, H. C., Von Randow, C., Aguiar, R. G., and Maia, J. F.: Patterns of water and heat fux across a biome gradient from tropical forest to savanna in Brazil, J. Geophys. Res.-Biogeo., 114, G00B12, doi:10.1029/2007JG000640, 2009.

De Jeu, R. A. M., Wagner, W., Holmes, T. R. H., Dolman, A. J., van de Giesen, N. C., and Friesen, J.: Global soil moisture patterns observed by space borne microwave radiometers and scatterometers, Surv. Geophys., 29, 399–420, 2008.

Desai, A. R., Bolstad, P. V., Cook, B. D., Davis, K. J., and Carey, E. V.: Comparing net ecosystem exchange of carbon dioxide between an old-growth and mature forest in the upper Midwest, USA, Agr. Forest Meteorol., 128, 33–55, 2005.

Dirmeyer, P. A., Gao, X. A., Zhao, M., Guo, Z. C., Oki, T., and Hanasaki, N.: GSWP-2 Multimodel anlysis and implications for our perception of the land surface, B. Am. Meteorol. Soc., 87, 1381–1397, 2006.

Global land-surface evaporation

D. G. Miralles et al.

Title Page

Abstract	Introduction
Conclusions	References
Tables	Figures

◄ | ►

◄ | ►

Back | Close

Full Screen / Esc

Printer-friendly Version

Interactive Discussion

Dolman, A. J. and De Jeu, R. A. M.: Evaporation in focus, Nat. Geosci., 3, 296, 2010.

Dolman, A. J. and Gash, J. H.: Evaporation in the global hydrological cycle, in: Treatise on Water Science, edited by: Wilderer, P., in press, vol. 2, ch. 5, Elsevier, 2010.

Dolman, A. J., Moors, E. J., and Elbers, J. A.: The carbon uptake of a mid latitude forest on sandy soil, Agr. Forest Meteorol., 111, 157–170, 2002.

Dow, C. L. and DeWalle, D. R.: Trends in evaporation and Bowen ratio on urbanizing watersheds in eastern United States, Water Resour. Res, 36, 1835–1843, 2000.

Eamus, D., Hutley, L. B., and O'Grady, A. P.: Daily and seasonal patterns of carbon and water fluxes above a north Australian savanna, Tree Physiol., 21, 977–988, 2001.

Ebert, E. E., Janowiak, J. E., and Kidd, C.: Comparison of near-real-time precipitation estimates from satellite observations and numerical models, B. Am. Meteorol. Soc., 88, 47–64, 2007.

FAO: Digital soil map of the world and derived soil properties, Rev. 1 (CD Rom), 1, FAO Land and Water Digital Media Series, at: http://www.fao.org/ag/agl/agll/dsmw.htm, last access: 21 October 2010, 2000.

Fisher, J. B., Tu, K. P., and Baldocchi, D. D.: Global estimates of the land-atmosphere water flux based on monthly AVHRR and ISLSCP-II data, validated at 16 FLUXNET sites, Remote Sens. Environ., 112, 901–919, 2008.

Gash, J. H.: An analytical model of rainfall interception by forests, Q. J. Roy. Meteorol. Soc., 105, 43–55, 1979.

Gash, J. H. and Stewart, J. B.: The evaporation from Thetford Forest during 1975, J. Hydrol., 35, 385–396, 1977.

Giasson, M. A., Coursolle, C., and Margolis, H. A.: Ecosystem-level CO_2 fluxes from a boreal cutover in eastern Canada before and after scarification, Agr. Forest Meteorol., 140, 23–40, 2006

Gilmanov, T. G., Soussana, J. F., Aires, L., Allard, V., Ammann, C., Balzarolo, M., Barcza, Z., Bernhofer, C., Campbell, C. L., Cernusca, A., Cescatti, A., Clifton-Brown, J., Dirks, B. O. M., Dore, S., Eugste, W., Fuhrer, J., Gimeno, C., Gruenwald, T., Haszpra, L., Hensen, A., Ibrom, A., Jacobs, A. F. G., Jones, M. B., Lanigan, G., Laurila, T., Lohila, A., Manca, G., Marcolla, B., Nagy, Z., Pilegaard, K., Pinter, K., Pio, C., Raschi, A., Rogiers, N., Sanz, M. J., Stefani, P., Sutton, M., Tuba, Z., Valentini, R., Williams, M. L., and Wohlfahrt, G.: Partitioning European grassland net ecosystem CO_2 exchange into gross primary productivity and ecosystem respiration using light response function analysis, Agr. Ecosyst. Environ., 121, 93–120, 2007.

Global land-surface evaporation

D. G. Miralles et al.

Title Page

Abstract	Introduction
Conclusions	References
Tables	Figures

Back | Close

Full Screen / Esc

Printer-friendly Version

Interactive Discussion

Gouweleeuw, B. T.: Satellite passive microwave surface moisture monitoring, a case-study on the impact of climate variability and land use change on the regional hydrogeology of the West La Mancha region in semi-arid central Spain, Ph.D. thesis, Vrije Universiteit Amsterdam, Ch. 4, 85–90, 2000.

5 Grünwald, T. and Berhofer, C.: A decade of carbon, water and energy flux measurements of an old spruce forest at the Anchor Station Tharandt, Tellus B, 59, 387–396, 2006.

Gu, L., Meyers, T., Pallardy, S. G., Hanson, P. J., Yang, B., Heuer, M., Hosman, K. P., Riggs, J. S., Sluss, D., and Wullschleger, S. D.: Direct and indirect effects of atmospheric conditions and soil moisture on surface energy partitioning revealed by a prolonged drought at 10 a temperate forest site, J. Geophys Res.-Atmos. 111, D16102, doi:10.1029/2006JD007161, 2006.

Hansen, M. C., Townshend, J. R. G., DeFries, R. S., and Carroll, M.: Estimation of tree cover using MODIS data at global, continental and regional/local scales, Int. J. Remote Sens., 26, 4359–4380, 2005.

15 Henderson-Sellers, B.: A new formula for latent heat of vaporization of water as a function of temperature, Q. J. Roy. Meteorol. Soc., 110, 1186–1190, 1984.

Hendriks, D. M. D., van Huissteden, J., Dolman, A. J., and van der Molen, M. K.: The full greenhouse gas balance of an abandoned peat meadow, Biogeosciences, 4, 411–424, doi:10.5194/bg-4-411-2007, 2007.

20 Holmes, T. R. H., De Jeu, R. A. M., Owe, M., and Dolman, A. J.: Land surface temperature from Ka band (37 GHz) passive microwave observations, J. Geophys. Res.-Atmos., 114, D04113, doi:10.1029/2008JD010257, 2009.

Howard, E. A., Gower, S. T., Foley, J. A., and Kucharik, C. J.: Effects of logging on carbon dynamics of a jack pine forest in Saskatchewan, Canada, Global Change Biol., 10, 1267–25 1284, 2004.

Huffman, G. J., Adler, R. F., Arkin, P., Chang, A., Ferraro, R., Gruber, A., Janowiak, J., McNab, A., Rudolf, B., and Schneider, U.: The Global Precipitation Climatology Project (GPCP) combined precipitation dataset, B. Am. Meteorol. Soc., 78, 5–20, 1997.

Huffman, G. J., Adler, R. F., Morrissey, M. M., Bolvin, D. T., Curtis, S., Joyce, R., McGavock, 30 B., and Susskind, J.: Global precipitation at one-degree daily resolution from multisatellite observations, J. Hydrometeorol., 2, 36–50, 2001.

Title Page

Abstract	Introduction
Conclusions	References
Tables	Figures

|◄ | ►|

◄ | ►

Back | Close

Full Screen / Esc

Printer-friendly Version

Interactive Discussion

Humphreys, E. R., Black, T. A., Morgenstern, K., Cai, T., Drewitt, G. B., Nesic, Z., and Trofymow, J. A.: Carbon dioxide fluxes in coastal Douglas-fir stands at different stages of development after clearcut harvesting, Agr. Forest Meteorol., 140, 6–22, 2006.

Jimenez, C., Prigent, C., and Aires, F.: Toward an estimation of global land surface heat fluxes from multisatellite observations, J. Geophys. Res.-Atmos., 114, D06305, doi:10.1029/2008JD011392, 2009.

Jimenez, C., Prigent, C., Mueller, B., Seneviratne, S. I., McCabe, M. F., Wood, E. F., Rossow, W. B., Balsamo, G., Betts, A. K., Dirmeyer, P. A., Fisher, J. B., Jung, M., Kanamitsu, M., Reichle, R. H., Reichstein, M., Rodell, M., Sheffield, J., Ku, T., and Wang, K.: Global inter-comparison of 12 land surface heat flux estimates, J. Geophys. Res.-Atmos., in review, 2010.

Joyce, R. J., Janowiak, J. E., Arkin, P. A., and Xie, P.: CMORPH: A method that produces global precipitation estimates from passive microwave and infrared data at high spatial and temporal resolution, J. Hydrometeorol., 5, 487–503, 2004.

Jung, M., Reichstein, M., and Bondeau, A.: Towards global empirical upscaling of FLUXNET eddy covariance observations: validation of a model tree ensemble approach using a biosphere model, Biogeosciences, 6, 2001–2013, doi:10.5194/bg-6-2001-2009, 2009.

Kelly, R. E. J., Chang, A. T. C., Tsang, L., and Foster, J. L.: A prototype AMSR-E global snow area and snow depth algorithm, IEEE T. Geosci. Remote, 41, 230–242, 2003.

Kirdiashev, K. P., Chukhlantsev, A. A., and Shutko, A. M.: Microwave radiation of the Earth's surface in the presence of vegetation, Radio Eng. Electron. P., 24, 256–264, 1979.

Knohl, A., Schulze, E. D., Kolle, O., and Buchmann, N.: Large carbon uptake by an unmanaged 250-year-old deciduous forest in Central Germany, Agr. Forest Meteorol., 118, 151–167, 2003.

Law, B. E., Turner, D. P., Sun, O., Van Tuyl, S., Ritts, W. D., and Cohen, W. B.: Disturbance and climate effects on carbon stocks and fluxes across western Oregon USA, Global Change Biol., 10, 1–16, 2004.

Mach, D. M., Christian, H. J., Blakeslee, R. J., Boccippio, D. J., and Goodman, S. J.: Performance assessment of the optical transient detector and lightning imaging sensor, J. Geophys. Res.-Atmos., 112, D09210, doi:10.1029/2006JD007787, 2007.

Matamala, R., Jastrow, J. D., Miller, R. M., and Garten, C. T.: Temporal changes in C and N stocks of restored prairie: Implications for C sequestration strategies, Ecol. Appl., 18, 1470–1488, 2008.

Meyers, T. P. and Hollinger, S. E.: An assessment of storage terms in the surface energy balance of maize and soybean, Agr. Forest Meteorol., 125, 105–116, 2004.

Miralles, D. G., Gash, J. H., Holmes, T. R. H., De Jeu, R. A. M., and Dolman, A. J.: Global canopy interception from satellite observations, J. Geophys. Res.-Atmos., 115, D16122, doi:10.1029/2009JD013530, 2010.

Moureaux, C., Debacq, A., Bodson, B., Heinesch, B., and Aubinet, M.: Annual net ecosystem carbon exchange by a sugar beet crop, Agr. Forest Meteorol., 139, 25–39, 2006.

Murphy, D. M. and Koop, T.: Review of the vapour pressures of ice and supercooled water for atmospheric applications, Q. J. Roy. Meteorol. Soc., 131, 1539–1565, 2005.

Noormets, A., Sun, G., McNulty, S. G., Gavazzi, M., Chen, J., Domec, J. C., King, J. S., Amatya, D. M., and Skaggs, R. W.: Corrigendum: Energy and water balances of two contrasting loblolly pine plantations on the lower coastal plain of North Carolina, USA, Forest Ecol. Manag., 259, 1299–1310, 2010.

Owe, M., De Jeu, R. A. M., and Holmes, T. R. H.: Multisensor historical climatology of satellite-derived global land surface moisture, J. Geophys. Res.-Earth, 113, F01002, doi:10.1029/2007JF000769, 2008.

Owe, M. and Van de Griend, A. A.: A daily surface moisture model for large area semi-arid land application with limited climate data, J. Hydrol., 121, 119–132, 1990.

Pintér, K., Barcza, Z., Balogh, J., Czóbel, S., Csintalan, Z., Tuba, Z., and Nagy, Z.: Interannual variability of grasslands' carbon balance depends on soil type, Community Ecol., 9, 43–48, 2008.

Poveda, G. and Mesa, O. J.: Feedbacks between hydrological processes in tropical South America and large-scale ocean-atmospheric phenomena, J. Climate, 10, 2690–2702, 1997.

Prescher, A.-K., Grünwald, T., and Bernhofer, C.: Land use regulates carbon budgets in eastern Germany: from NEE to NBP, Agr. Forest Meteorol., 150, 1016–1025, 2010.

Priestley, C. H. B. and Taylor, R. J.: On the assessment of surface heat flux and evaporation using large-scale parameters, Mon. Weather Rev., 100, 81–92, 1972.

Rebmann, C., Zeri, M., Lasslop, G., Mund, M., Kolle, O., Schulze, E. D., and Feigenwinter, C.: Treatment and assessment of the CO_2-exchange at a complex forest site in Thuringia, Germany, Agr. Forest Meteorol., 150, 684–691, 2010.

Reichle, R. H.: Data assimilation methods in the Earth sciences, Adv. Water Resour., 31, 1411–1418, 2008.

Title Page

Abstract | Introduction

Conclusions | References

Tables | Figures

|◀ | ▶|

◀ | ▶

Back | Close

Full Screen / Esc

Printer-friendly Version

Interactive Discussion

Schaefer, G. L., Cosh, M. H., and Jackson, T. J.: The USDA Natural Resource Conservation Service Soil Analysis Network (SCAN), J. Atmos. Ocean. Tech., 24, 2073–2077, 2007.

Schindler, D., Türk, M., and Mayer, H.: CO_2 fluxes of a Scots pine forest growing in the warm and dry southern upper Rhine plain, SW Germany, Eur. J. Forest Res., 125, 201–212, 2005.

Scott, R. L., Hamerlynck, E. P., Jenerette, G. D., Moran, M. S., and Barron-Gafford, G.: Carbon dioxide exchange in a semidesert grassland through drought-induced vegetation change, J. Geophys. Res.-Biogeo., 115, G03026, doi:10.1029/2010JG001348, 2010.

Scott, R. L., Jenerette, G. D., Potts, D. L., and Huxman, T. E.: Effects of seasonal drought on net carbon dioxide exchange from a woody-plant-encroached semiarid grassland, J. Geophys. Res.-Biogeo., 114, G04004, doi:10.1029/2008JG000900, 2009.

Shepard, D.: A two-dimensional interpolation function for irregularly-spaced data, Proceedings of the 1968 23rd ACM National Conference, 517–524, 1968.

Shuttleworth, W. J. and Calder, I. R.: Has the Priestley-Taylor equation any relevance to forest evaporation?, J. Appl. Meteorol., 18, 639–646, 1979.

Shuttleworth, W. J., Gash, J. H., Lloyd, C. R., Moore, C. J., Roberts, J., de O. Marques, A., Fisch, G., de P. Silva, V., Ribeiro, M. D. N. G., Molion, L. C. B., de Sá, L. D. A., Nobre, J. C., Cabral, O. M. R., Patel, S. R., and de Moraes, J. C.: Eddy correlation measurements of energy partition for Amazonian forest, Q. J. Roy. Meteorol. Soc, 110, 1143–1162, 1984.

Sun, G., Noormets, A., Gavazzi, M., McNulty, S. G., Chen, J., Domec, J. C., King, J. S., Amatya, D. M., and Skaggs, R. W.: Energy and water balances of two contrasting loblolly pine plantations on the lower coastal plain of North Carolina, USA, Forest Ecol. Manag., 259, 1299–1310, 2010.

Suni, T., Berninger, F., Vesala, T., Markkanen, T., Hari, P., Mäkelä, A., Ilvesniem, H., Hänninen, H., Nikinmaa, E., Huttula, T., Laurila, T., Aurela, M., Grelle, A., Lindroth, A., Arneth, A., Shibistova, O., and Lloyd, J.; Air temperature triggers the recovery of evergreen boreal forest photosynthesis in spring, Global Change Biol., 9, 1410–1426, 2003a.

Suni, T., Rinne, J., Reissell, A., Altimir, N., Keronen, P., Rannik, Ü., Maso, M. D., Kulmala, M., and Vesala, T.: Long-term measurements of surface fluxes above a Scots pine forest in Hyytiälä, southern Finland, 1996–2001, Boreal Environ. Res., 8, 287–301, 2003b.

Taylor, K. E.: Summarizing multiple aspects of model performance in a single diagram, J. Geophys. Res., 106, 7183–7192, 2001.

Title Page

Abstract	Introduction
Conclusions	References
Tables	Figures

|◀ | ▶|

◀ | ▶

Back | Close

Full Screen / Esc

Printer-friendly Version

Interactive Discussion

Valente, F., David, J. S., and Gash, J. H.: Modelling interception loss for two sparse eucalypt and pine forests in central Portugal using reformulated Rutter and Gash analytical models, J. Hydrol., 190, 141–162, 1997.

Wohlfahrt, G., Hammerle, A., Haslwanter, A., Bahn, M., Tappeiner, U., and Cernusca, A.: Seasonal and inter-annual variability of the net ecosystem CO_2 exchange of a temperate mountain grassland: Effects of weather and management, J. Geophys. Res.-Atmos., 113, D08110, doi:10.1029/2007JD009286, 2008.

Zeweldi, D. A. and Gebremichael, M.: Evaluation of CMORPH precipitation products at fine space-time scales, J. Hydrometeorol., 10, 300–308, 2009.

Zhang, Y., Rossow, W. B., Lacis, A. A., Oinas, V., and Mishchenko, M. I.: Calculation of radiative fluxes from the surface to top of atmosphere based on ISCCP and other global data sets: Refinements of the radiative transfer model and the input data, J. Geophys. Res., 109, D19105, doi:10.1029/2003JD004457, 2004.

Table 1. Remotely sensed data sets used for computing GLEAM E estimates (see Sect. 3 for explanation of abbreviations).

Variables	Source	Freq.	Domain	Availability	Res.	Method
Net Radiation, R_n	SRB	Daily	Global	1983–2007	1°	Satellite/Reanalysis
Precipitation, P	CMORPH	Daily	60° N–60° S	2002–2009	0.07°	Satellite
Precipitation, P (gap-filling)	GPCP	Daily	Global	1997–2008	1°	Satellite/Gauges
Surface Soil Moisture, θ	LPRM	Daily	Global	1979–2009	0.25°	Satellite
Land Surface Temperature, T	LPRM	Daily	Global	1979–2009	0.25°	Satellite
Air Temperature, T (gap-filling)	ISCCP	3-hourly	Global	1983–2008	2.5°	Satellite
Vegetation density, τ	LPRM	Daily	Global	1979–2009	0.25°	Satellite
Snow water equivalents, D_s	NSIDC	Daily	Global	2002–2009	0.25°	Satellite

Table 2. SCAN study sites and results of the validation of the modelled soil moisture profile.

SCAN station	Land cover	Lat.	Long.	First layer		Second layer	
				$R_{w/o\ DA}$	$R_{w/DA}$	$R_{w/o\ DA}$	$R_{w/DA}$
Abrams – KS	Grassland	37.12	−97.08	0.48	0.55	0.69	0.74
Allen Farms – TN	Grassland	35.07	−86.90	0.69	0.71	0.86	0.87
Bushland – TX	Grassland	35.17	−102.1	0.64	0.78	0.79	0.89
Dewitt – AR	Cultivated grass	34.28	−91.34	0.39	0.56	0.48	0.60
Dexter – MO	Cultivated grass	36.78	−89.94	0.55	0.59	0.50	0.50
Eastview Farm – TN	Grass/bare	35.13	−86.19	0.68	0.68	0.80	0.80
Fort Assiniboine – MT	Cropland	48.48	−109.8	0.47	0.47	0.54	0.46
Fort Reno – OK	Shrubland	35.55	−98.02	0.33	0.53	0.50	0.60
Geneva – NY	Grassland	42.88	−77.30	0.60	0.60	0.78	0.78
Hartselle USDA – AL	Grassland	34.43	−87.00	0.72	0.72	0.77	0.76
Isabela – PR	Grassland	18.47	−67.05	0.39	0.39	0.50	0.50
Lind – WA	Mixed grassland	47.00	−118.56	0.57	0.64	0.76	0.76
Little River – GA	Cultivated grass	31.50	−83.55	0.69	0.67	0.77	0.80
LynHart Ranch – OR	Grass/bare	42.02	−121.35	0.37	0.43	0.65	0.69
Mammoth Cave – KY	Grass/bare	37.18	−86.03	0.64	0.64	0.76	0.76
Mt. Vernon – MO	Grass/bare	37.06	−93.90	0.73	0.73	0.80	0.81
N Piedmont AREC – VA	Cultivated grass	38.23	−78.11	0.56	0.56	0.67	0.67
Nunn – CO	Grassland	40.89	−104.73	0.37	0.44	0.51	0.53
Prairie View – TX	Grassland	30.07	−95.98	0.60	0.70	0.71	0.75
Princeton – KY	Grassland	37.10	−87.83	0.70	0.70	0.83	0.83
Reynolds Homestead – VA	Grassland	36.63	−80.13	0.59	0.59	0.68	0.68
Reynolds Creek – ID	Shrubland	43.07	−116.75	0.74	0.74	0.82	0.85
Rock Springs – PA	Cultivated grass	40.72	−77.94	0.62	0.61	0.93	0.93
Shagbark Hills – ID	Grassland	42.43	−95.77	0.19	0.16	0.16	0.17
Shenandoah – VA	Grassland	37.93	−79.20	0.74	0.74	0.83	0.83
Starkville – MS	Grassland	33.64	−88.77	0.64	0.67	0.69	0.69
Tidewater AREC – VA	Cultivated grass	36.68	−76.76	0.62	0.71	0.81	0.87
UAPB Point Remove – AR	Grass/bare	35.22	−92.92	0.53	0.58	0.71	0.73
Vance – MS	Grassland	34.07	−90.34	0.50	0.44	0.69	0.58
Walnut Gulch – AZ	Shrubland	31.73	−110.05	0.69	0.63	0.57	0.39
Mean				0.57	0.60	0.68	0.69
Median				0.60	0.62	0.71	0.74

Global land-surface evaporation

D. G. Miralles et al.

Title Page

Abstract | Introduction

Conclusions | References

Tables | Figures

◄ | ►|

◄ | ►

Back | Close

Full Screen / Esc

Printer-friendly Version

Interactive Discussion

Discussion Paper | Discussion Paper | Discussion Paper | Discussion Paper

Table 3. List of the 43 FLUXNET sites used in the validation of E estimates. The correlation coefficients with E GLEAM for the daily and monthly time series are listed (in situ R_n used).

station	Reference/Primary contact	Lat.	Long.	Land cover	Group	R (day)	R (month)
AT-Neu	Wohlfahrt et al. (2008)	47.12	11.32	Montane grassland	C	0.92	0.98
AU-How	Eamus et al. (2001)	−12.49	131.15	Tropical savannah	A	0.74	0.88
BE-Lon	Moureaux et al. (2006)	50.55	4.74	Cropland	D	0.88	0.94
BR-Ban	Da Rocha et al. (2009)	−9.82	−50.16	Tropical forest	A	0.42	0.01
CA-Ca1	Humphreys et al. (2006)	49.87	−125.33	Douglas fir forest	A	0.84	0.94
CA-Ca2	Humphreys et al. (2006)	49.87	−125.29	Harvested Douglas fir	C	0.92	0.98
CA-Ojp	Howard et al. (2004)	53.92	−104.69	Mixed boreal forest	A	0.81	0.91
CA-Qcu	Giasson et al. (2006)	49.27	−74.04	Boreal shrubland	D	0.91	0.97
CA-Qfo	Bergeron et al. (2007)	49.69	−74.34	Conifer forest	B	0.78	0.85
CH-Oe1	Ammann et al. (2007)	47.29	7.73	Grassland	C	0.95	0.99
CN-Xfs	Guangsheng Zhou	44.13	116.33	Grassland	D	0.76	0.89
DE-Geb	Anthoni et al. (2004)	51.10	10.91	Cropland	D	0.90	0.98
DE-Hai	Knohl et al. (2003)	51.08	10.45	Deciduous forest	B	0.93	0.96
DE-Har	Schindler et al. (2005)	47.93	7.60	Pine forest	A	0.88	0.97
DE-Kli	Prescher et al. (2010)	50.89	13.52	Cropland	D	0.91	0.97
DE-Meh	Axel Don	51.28	10.66	Grassland	D	0.94	0.99
DE-Tha	Grünwald and Bernhofer (2007)	50.96	13.57	Coniferous forest	B	0.88	0.96
DE-Wet	Rebmann et al. (2010)	50.45	11.56	Coniferous forest	B	0.88	0.91
ES-LMa	Casal et al. (2009)	39.94	−5.77	Evergreen sparse forest	B	0.77	0.93
ES-VDA	Gilmanov et al. (2007)	42.15	1.45	Grassland	D	0.83	0.93
FI-Hyy	Suni et al. (2003b)	61.85	24.29	Coniferous forest	B	0.89	0.93
FI-Sod	Suni et al. (2003a)	67.36	26.64	Coniferous forest	A	0.72	0.90
FR-Lam	Ceschia Eric	43.49	1.24	Cropland	C	0.65	0.74
HU-Bug	Gilmanov et al. (2007)	46.69	19.60	Grassland	C	0.93	0.97
HU-Mat	Pintér et al. (2008)	47.85	19.73	Grassland	C	0.92	0.97
IT-Amp	Gilmanov et al. (2007)	41.90	13.61	Grassland	C	0.83	0.91
NL-Hor	Hendriks et al. (2007)	52.03	5.07	Grassland	D	0.87	0.98
NL-Loo	Dolman et al. (2002)	52.17	5.74	Coniferous forest	B	0.73	0.95
PT-Mi2	Gilmanov et al. (2007)	38.48	−8.02	Grassland	D	0.69	0.85
RU-Fyo	Andrej Varlagin	56.46	32.92	Mixed forest	B	0.92	0.97
US-ARc	Margaret Torn	35.54	−98.04	Grassland	C	0.94	0.98
US-Aud	Tilden P. Meyers	31.59	−110.51	Desert grassland	C	0.84	0.88
US-Bo1	Meyers et al. (2004)	40.01	−88.29	Cropland	C	0.84	0.94
US-Goo	Tilden P. Meyers	34.25	−89.97	Grassland/shrubland	C	0.78	0.90
US-IB2	Matamala et al. (2008)	41.84	−88.24	Grassland	D	0.90	0.98
US-Me2	Law et al. (2004)	44.45	−121.56	Coniferous forest	A	0.80	0.87
US-MOz	Gu et al. (2006)	38.74	−92.20	Oak forest	A	0.88	0.96
US-NC1	Sun et al. (2010); Noormets et al. (2010)	35.81	−76.71	Pine, young plantation	C	0.90	0.97
US-SRM	Scott et al. (2009)	31.82	−110.87	Shrubland/savannah	C	0.86	0.92
US-Syv	Desai et al. (2005)	46.24	−89.35	Mature broadleaf forest	A	0.91	0.95
US-Ton	Baldocchi et al. (2004)	38.43	−120.97	Oak savanna/grassland	B	0.89	0.96
US-WCr	Cook et al. (2004)	45.81	90.08	Mixed forest	A	0.88	0.91
US-Wkg	Scott et al. (2010)	31.74	−109.94	Grassland/shrubland	D	0.71	0.87
Mean						0.84	0.91

Global land-surface evaporation

D. G. Miralles et al.

Title Page

Abstract	Introduction
Conclusions	References
Tables	Figures

|◄ | ►|

◄ | ►

Back | Close

Full Screen / Esc

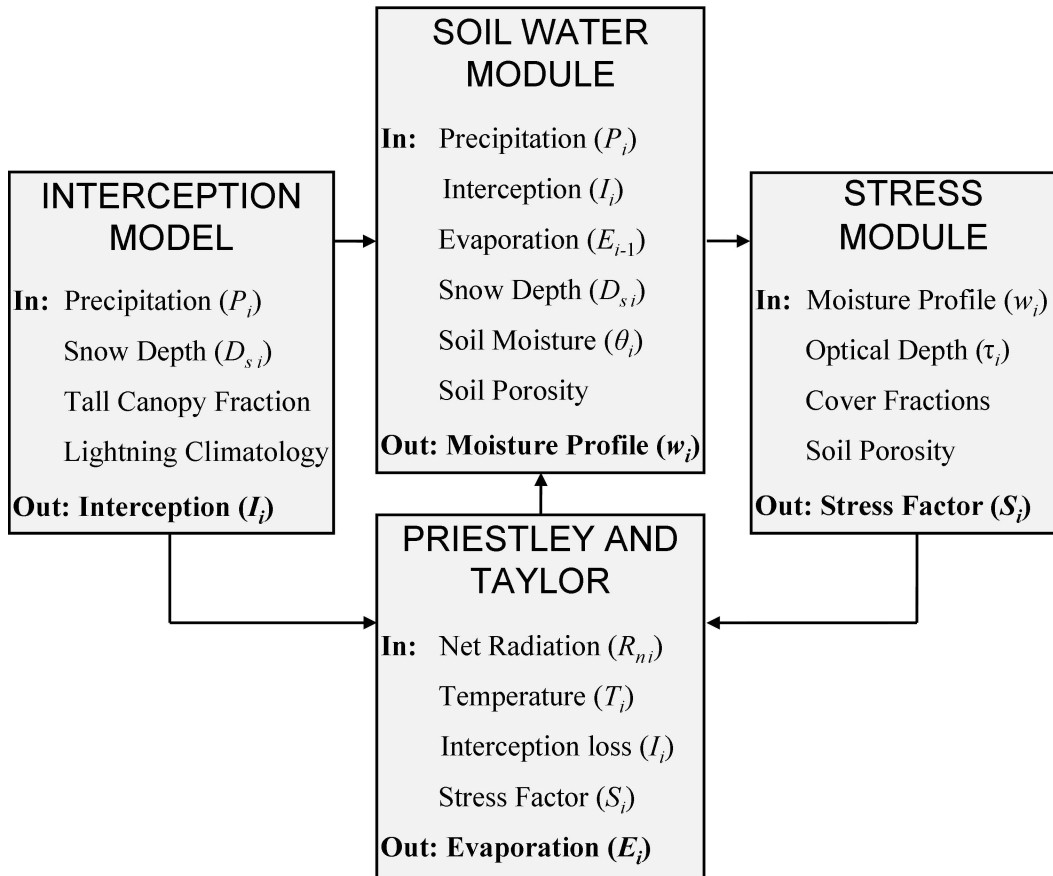Printer-friendly Version

Interactive Discussion

Fig. 1. Schematic overview of GLEAM for a given day (i).
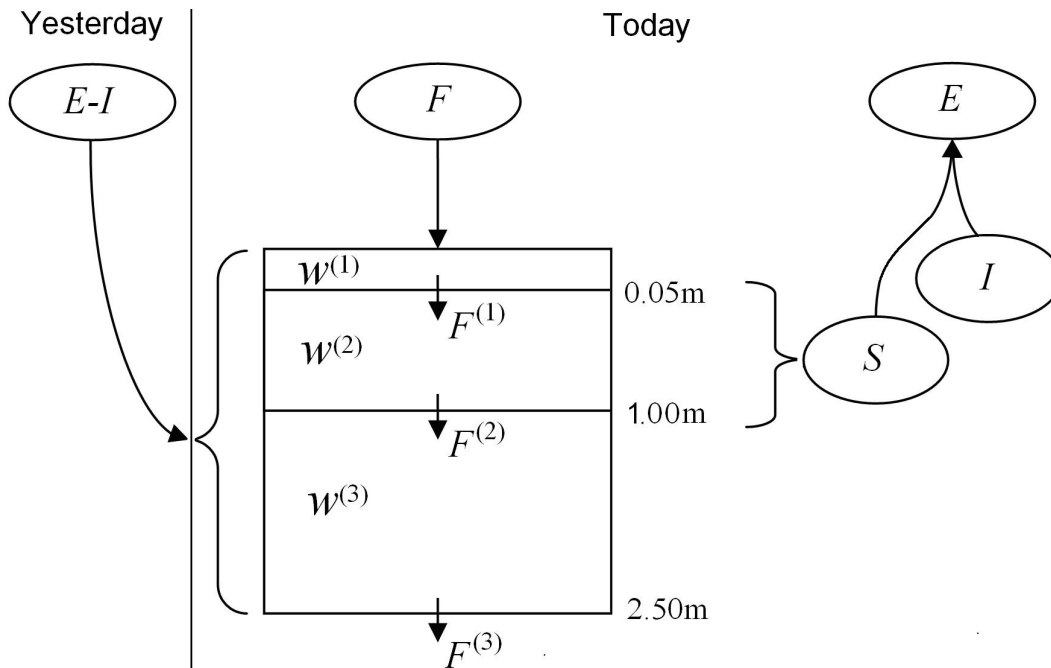
Fig. 2. Schematic overview of the running water balance for the fraction of tall canopy (three layer profile). In this example, the second layer is the wettest layer and therefore it determines the stress factor, S (see Sect. 2.3).

Title Page

Abstract	Introduction
Conclusions	References
Tables	Figures

|◀ | ▶|

◀ | ▶

Back | Close

Full Screen / Esc

Printer-friendly Version

Interactive Discussion

Tall Canopy:

$$S = 1 - \left(\frac{w_c - w_w}{w_c - w_{wp}}\right)^2$$

Herbaceous:

$$S = \frac{1 - \sqrt{\frac{w_c - w_w}{w_c - w_{wp}}} + \frac{\tau}{0.8}}{2}$$

Bare Soil:

$$S = 1 - \sqrt{\frac{w_c - w_w}{w_c - w_{wp}}}$$
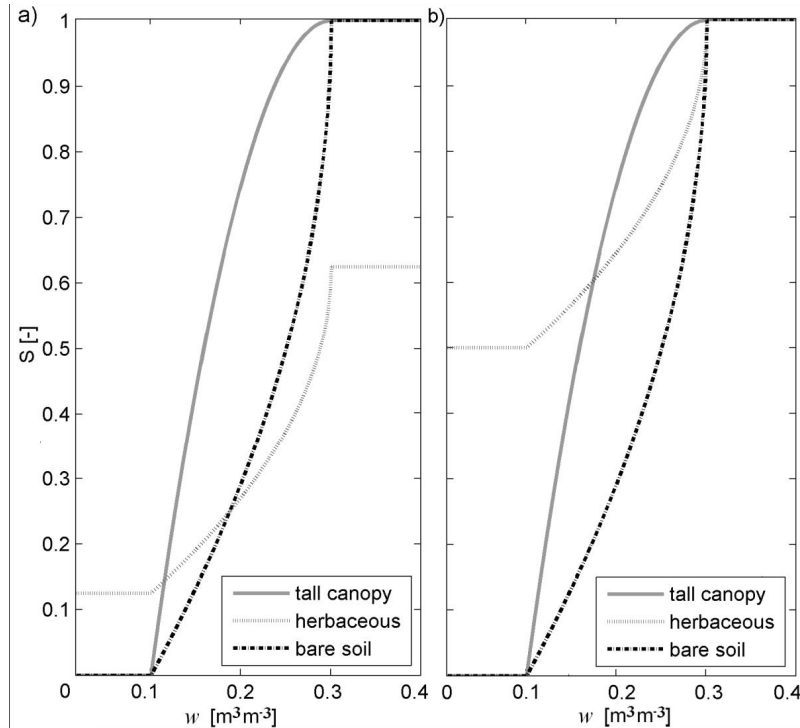
Fig. 3. Overview of stress parameterisations for tall canopy, short vegetation, and bare land, illustrated at two levels of vegetation density: **(a)** $\tau = 0.2$, **(b)** $\tau = 0.8$. The values of w_{wp} and w_c are considered to be 0.1 and 0.3 $m^3 m^{-3}$ respectively; w_w corresponds to the soil moisture modelled for the wettest layer.
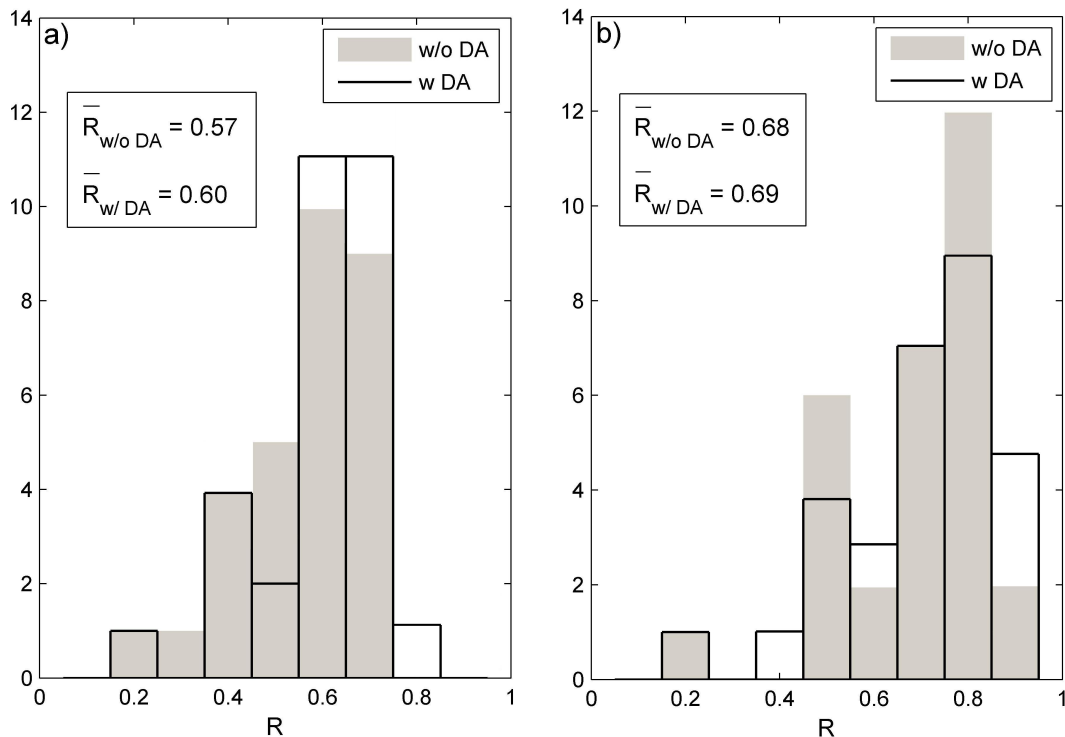
Fig. 4. Histograms of the correlation coefficient (R) of the model soil water content with in situ SCAN data for: **(a)** first layer of soil, **(b)** second layer of soil. The histograms show the difference in the validation with and without the data assimilation (DA) of satellite soil moisture.

Title Page

Abstract | Introduction

Conclusions | References

Tables | Figures

◄◄ | ►►

◄ | ►

Back | Close

Full Screen / Esc

Printer-friendly Version

Interactive Discussion

a)

b)
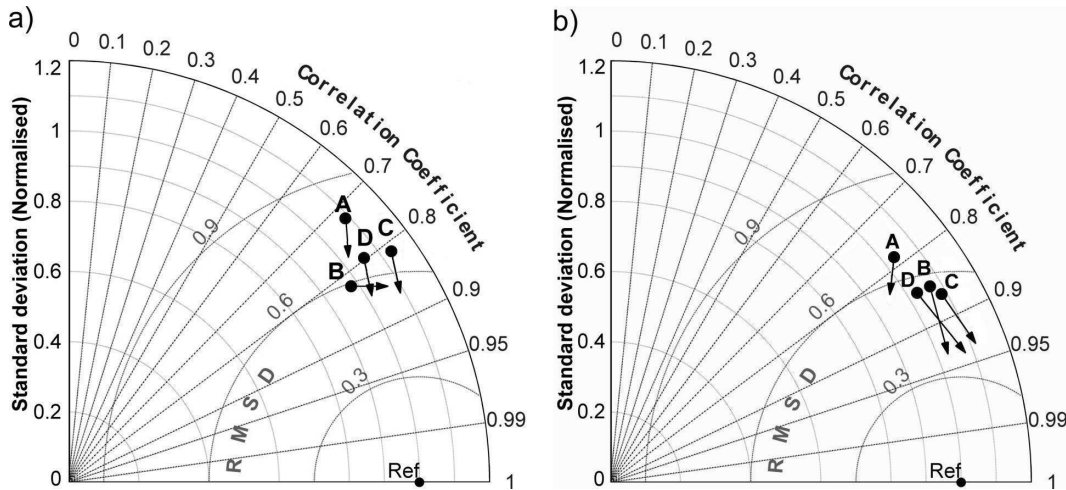
Fig. 5. Taylor diagrams of the validation results for the groups listed in Table 3. RMSD and standard deviation are normalised against the reference represented by the time series of the corresponding FLUXNET station; therefore, the point denoted as "Ref" represents the location in the diagram of the time series of every station. **(a)** shows the results of the comparison between daily time series of modelled E and the E measured at the 43 FLUXNET stations. The dots correspond to the statistics of the model run with the satellite R_n as input; the arrows point the results of the model validation when using the R_n measured at the stations as input. **(b)** shows how the statistics improve when comparing monthly averages instead of daily time series (using the station R_n as input).
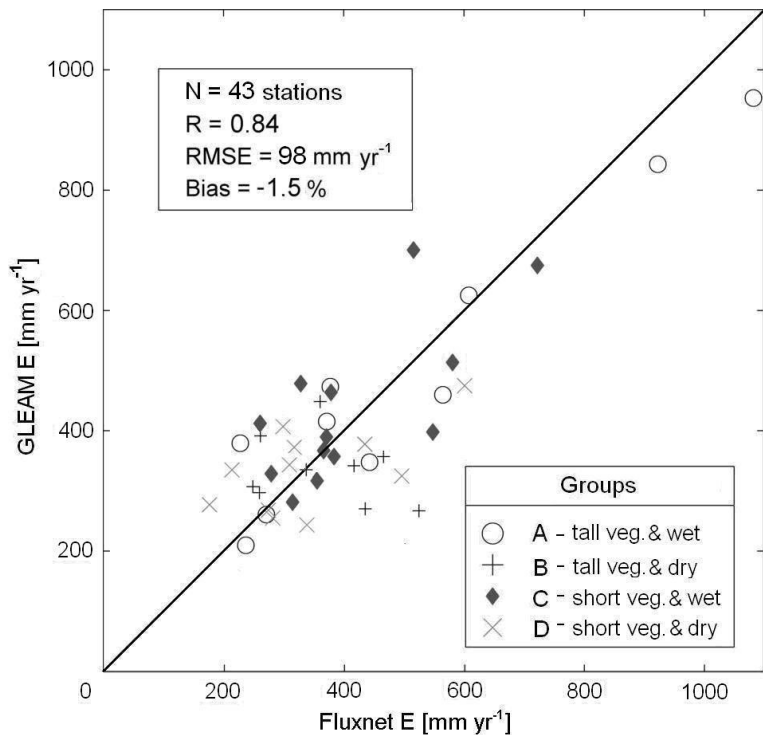
Fig. 6. GLEAM annual E for the year 2005 against annual cumulative evaporation from the 43 FLUXNET stations for the same year. Stations are grouped by vegetation cover and climate conditions (see Sect. 4.2.1).
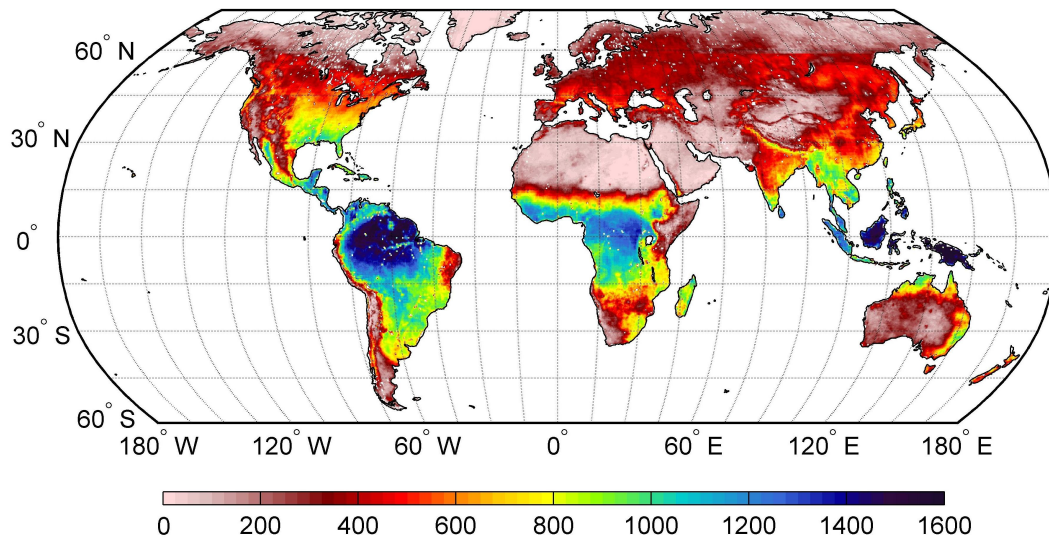
Fig. 7. GLEAM E for 2005 (in mm).